The Astrophysical Journal, 863:193 (15pp), 2018 August 20 https://doi.org/10.3847/1538-4357/aad2e0

Molecular Gas Filaments and Star-forming Knots Beneath an X-Ray Cavity in RXC J1504–0248

A. N. Vantyghem[1], B. R. McNamara[1,2], H. R. Russell[3], A. C. Edge[4], P. E. J. Nulsen[5,6], F. Combes[7,8], A. C. Fabian[3], M. McDonald[9], and P. Salomé[7]

[1] Department of Physics and Astronomy, University of Waterloo, Waterloo, ON N2L 3G1, Canada; a2vantyg@uwaterloo.ca
[2] Perimeter Institute for Theoretical Physics, Waterloo, ON, Canada
[3] Institute of Astronomy, Madingley Road, Cambridge CB3 0HA, UK
[4] Department of Physics, Durham University, Durham DH1 3LE, UK
[5] Harvard-Smithsonian Center for Astrophysics, 60 Garden Street, Cambridge, MA 02138, USA
[6] ICRAR, University of Western Australia, 35 Stirling Highway, Crawley, WA 6009, Australia
[7] LERMA, Observatoire de Paris, PSL Research University, Collège de France, CNRS, Sorbonne University, UPMC, Paris, France
[8] Collège de France, 11 place Marcelin Berthelot, F-75005 Paris, France
[9] Kavli Institute for Astrophysics and Space Research, Massachusetts Institute of Technology, 77 Massachusetts Avenue, Cambridge, MA 02139, USA
Received 2018 May 22; revised 2018 July 4; accepted 2018 July 9; published 2018 August 23

Abstract

We present recent ALMA observations of the CO (1–0) and CO (3–2) emission lines in the brightest cluster galaxy of RXC J1504.1−0248, which is one of the most extreme cool core clusters known. The central galaxy contains $1.9 \times 10^{10}\,M_{\odot}$ of molecular gas. The molecular gas morphology is complex and disturbed, showing no evidence for a rotationally supported structure in equilibrium. A total of 80% of the gas is situated within the central 5 kpc of the galactic center, while the remaining gas is located in a 20 kpc long filament. The cold gas has likely condensed out of the hot atmosphere. The filament is oriented along the edge of a putative X-ray cavity, suggesting that active galactic nucleus activity has stimulated condensation. This is energetically feasible, although the morphology is not as conclusive as systems whose molecular filaments trail directly behind buoyant radio bubbles. The velocity gradient along the filament is smooth and shallow. It is only consistent with freefall if it lies within 20° of the plane of the sky. The abundance of clusters with comparably low velocities suggests that the filament is not freefalling. Both the central gas and filamentary gas are coincident with bright UV emission from ongoing star formation. Star formation near the cluster core is consistent with the Kennicutt–Schmidt law. The filament exhibits increased star formation surface densities, possibly resulting from either the consumption of a finite molecular gas supply or spatial variations in the CO-to-H_2 conversion factor.

Key words: galaxies: active – galaxies: clusters: individual (RXC J1504.1–0248) – galaxies: ISM – galaxies: kinematics and dynamics

1. Introduction

Brightest cluster galaxies (BCGs) are the most massive galaxies in the universe. Those located at the centers of cool core clusters exhibit filamentary nebulae that span five orders of magnitude in temperature (Werner et al. 2013). The filaments contain massive molecular gas (∼100 K) reservoirs (Edge 2001; Edge et al. 2002; Edge & Frayer 2003; Salomé & Combes 2003), warm (10^4 K), ionized gas (e.g., Lynds 1970; Heckman 1981; Cowie et al. 1983; Hu et al. 1985; Crawford et al. 1999), and hot (10^7 K) gas emitting soft X-rays (e.g., Fabian et al. 2001, 2003; Werner et al. 2013; Walker et al. 2015). Star formation in these systems proceeds at rates of up to $10^3\,M_{\odot}\,\mathrm{yr}^{-1}$ (e.g., McNamara 2004; O'Dea et al. 2008; McDonald et al. 2011; Donahue et al. 2015; Tremblay et al. 2015) and is correlated with the intracluster medium (ICM) mass deposition rate (O'Dea et al. 2008). These signatures of cold gas are observed preferentially in systems in which the central cooling time of the ICM falls below 1 Gyr, or equivalently when the central entropy falls below 30 keV cm^2 (Cavagnolo et al. 2008; Rafferty et al. 2008; Werner et al. 2014; Pulido et al. 2017). The presence of this cooling time threshold indicates that cold gas is formed by condensation from the hot cluster atmosphere.

Despite the strong evidence for cold gas condensing out of the ICM, the observed molecular gas masses and star formation rates (SFRs) in BCGs are an order of magnitude lower than those expected from uninhibited cooling. It is now widely accepted that energetic feedback from active galactic nuclei (AGN) offset radiative losses, regulating the rate of ICM cooling (see McNamara & Nulsen 2007, 2012 for a review). High-resolution X-ray imaging has revealed bubbles (cavities) in the hot cluster atmosphere that were inflated by radio jets launched by the AGN. The sizes and confining pressure of these cavities provide a direct estimate of the average power output by the AGN. The jet power is closely coupled to the cooling rate of the cluster atmosphere in a large sample of galaxy groups and clusters (Bîrzan et al. 2004; Dunn & Fabian 2006; Rafferty et al. 2006), indicating that AGN are capable of preventing the majority of the hot gas from condensing.

Molecular gas is expected to play a crucial role in the AGN feedback cycle, as it connects gas condensation on large scales to accretion onto the nuclear supermassive black hole. Ram pressure from molecular clouds traveling through the ICM and collisions between clouds both provide natural mechanisms for cold clouds to shed their angular momentum and accumulate at the centers of BCGs (Pizzolato & Soker 2005, 2010). Simulations suggest that cold clouds condense from nonlinear overdensities in the ICM that are generated by cycles of AGN feedback and proceed to rain onto the central galaxy

(Gaspari et al. 2012, 2013; McCourt et al. 2012; Sharma et al. 2012; Li & Bryan 2014).

Observations have also demonstrated a link between molecular gas and AGN. Nebular emission in BCGs is typically confined to filaments that extend radially from the cluster core (e.g., Conselice et al. 2001; Hatch et al. 2006; McDonald et al. 2012). In the Perseus Cluster, two prominent nebular filaments are coincident with soft X-rays (Fabian et al. 2003), molecular hydrogen (Hatch et al. 2005; Lim et al. 2012), and CO emission (Salomé et al. 2006, 2011) and extend toward an X-ray cavity. Similar morphologies are observed in the nebular emission in several BCGs (e.g., Werner et al. 2011; Canning et al. 2013). ALMA observations have revealed molecular filaments trailing X-ray cavities in other BCGs (McNamara et al. 2014; Russell et al. 2016, 2017; Vantyghem et al. 2016). This gas either has been lifted directly from the cluster core by buoyantly rising radio bubbles or has cooled in situ from hot gas that has been uplifted to an altitude where it becomes thermally unstable (Revaz et al. 2008; McNamara et al. 2016).

In this work, we examine the molecular gas in RXC J1504.1–0248 BCG (hereafter RXC J1504) using new ALMA observations of the CO (1–0) and CO (3–2) emission lines. CO is the most common molecule used to observe molecular gas. The main constituent of molecular gas, H_2, is a symmetric molecule, so it does not possess the dipolar transitions used to observe cold ($\sim$20 K) gas (e.g., Bolatto et al. 2013). The two observed CO transitions provide differing resolutions and field of views, with CO (1–0) tracing larger-scale gas and CO (3–2) showing finer structure.

RXC J1504, at redshift $z = 0.2169$, is one of the most massive cool core clusters known. It is also compact, leading to an extremely bright X-ray core. A classical cooling flow model yields a mass deposition rate of 1500–1900 $M_\odot$ yr^{-1} (Böhringer et al. 2005). The molecular gas mass, $3 \times 10^{10}\,M_\odot$, obtained from IRAM 30 m CO (1–0) observations (A. C. Edge 2018, private communication), and SFR, 140 $M_\odot$ yr^{-1} (Ogrean et al. 2010), are also among the highest known. These factors indicate that RXC J1504 is experiencing a cycle of extreme cooling and is therefore a prime target for studying the connection between molecular gas and AGN feedback.

Throughout this paper, we assume a standard ΛCDM cosmology with $H_0 = 70$ km s^{-1} Mpc^{-1}, $\Omega_{m,0} = 0.3$, and $\Omega_{\Lambda,0} = 0.7$. At the redshift of RXC J1504 ($z = 0.216902$; SDSS Collaboration et al. 2017), the angular scale is $1'' = 3.5$ kpc and the luminosity distance is 1073 Mpc.

2. Observations and Data Reduction

The BCG of the RXC J1504.1–0248 galaxy cluster (R.A.: 15:04:07.503, decl.: −2:48:17.04) was observed by ALMA Bands 3 and 7 (Cycle 4, ID 2016.1.01269.S, PI McNamara), centered on the CO (1–0) and CO (3–2) lines at 94.725 and 284.161 GHz, respectively. The CO (1–0) observations were divided into four blocks, two of which were taken on 2016 October 27 and the others on 2016 November 2 and 2017 May 10. The total on-source integration time was 151 minutes. The CO (3–2) observation was conducted in a single block on 2017 July 4, with a total on-source integration time of 34 minutes. Each observation was split into $\sim$6-minute on-source integrations interspersed with observations of the phase calibrator. The observations used a single pointing centered on the BCG nucleus with a primary beam of 65″ at CO (1–0) and 22″ at CO (3–2). The CO (1–0) observations used between 38 and 47 antennas with baselines ranging from 16 to 1124 m, and the CO (3–2) observation used 45 antennas with baselines from 21 to 2650 m. The frequency division correlator mode was used for the CO spectral line observations, providing a 1.875 GHz bandwidth with 488 kHz frequency resolution. This corresponds to a velocity resolution of 1.5 km s^{-1} at CO (1–0) and 0.5 km s^{-1} at CO (3–2), although the data were smoothed to coarser velocity channels for subsequent analysis. An additional three basebands with the time division correlator mode, each with a 2 GHz bandwidth and frequency resolution of 15.625 MHz, were employed for each spectral line in order to measure the submillimeter continuum.

The observations were calibrated in CASA version 4.7.0 (McMullin et al. 2007) using the pipeline reduction scripts. Continuum-subtracted data cubes were created using UVCONTSUB and CLEAN. Additional phase self-calibration provided a 50% increase in the signal-to-noise ratio of the continuum at CO (1–0) and a 30% increase at CO (3–2). Images of the line emission were reconstructed using Briggs weighting with a robust parameter of 0.5. An additional *uv* tapering was used to smooth the CO (3–2) image on scales below 0.″1. The synthesized beams of the final CO (1–0) and CO (3–2) data cubes were 0.71 × 0.″61 (P.A. = −77°) and 0.25 × 0.″19 (P.A. = −57°), respectively. The data cubes were binned to velocity resolutions of 20 and 10 km s^{-1}, respectively, and the rms noise in line-free channels was 0.2 and 0.65 mJy beam^{-1}, respectively. Images of the continuum were created by combining line-free spectral channels from each baseband. We detected a continuum source located near the BCG nucleus with a flux density of 8.734 ± 0.015 mJy at 101.7945 GHz and 5.462 ± 0.045 mJy at 291.4581 GHz. Imaging the continuum in narrow velocity channels (2 km s^{-1}) shows no evidence of line absorption against the continuum emission.

The gas velocities reported here are measured in the rest frame of the BCG, with $z = 0.216902 \pm 0.000016$ (SDSS Collaboration et al. 2017). This redshift was measured using optical emission lines, so it traces the nebular gas within the BCG. Stellar absorption line measurements would provide a more robust tracer of the BCG systemic velocity. Gas motions may be affected by nongravitational processes, such as turbulence, whereas stellar motion is a direct tracer of the gravity of the BCG. An earlier SDSS data release provided an absorption-line-only measurement of the BCG velocity (Abazajian et al. 2004). This differs from the aforementioned value by only 30 km s^{-1}, which is well below the accuracy of the absorption measurement (150 km s^{-1}).

Throughout this work we compare the ALMA images with archival UVIS F689m and ACS F165LP images from the *Hubble Space Telescope* (*HST*). Each of these images is mutually offset and so has been shifted to align with the ALMA CO (3–2) image. The ALMA CO (1–0) and CO (3–2) images used the same phase calibrator, so the locations of the continuum source in the BCG nucleus are consistent. Identifying the centroids of the F689m and F165LP images is difficult, as they both contain filamentary continuum emission near the galactic nucleus. Fortunately, an additional point source (R.A.: 15:04:07.2782, decl.: −2:48:10.0075) was detected in the ALMA imaging, with a flux density of 79 ± 11 μJy at 101.7945 GHz. This emission originates from a galaxy located 7.″4 NW of the BCG. The *HST* F689m image

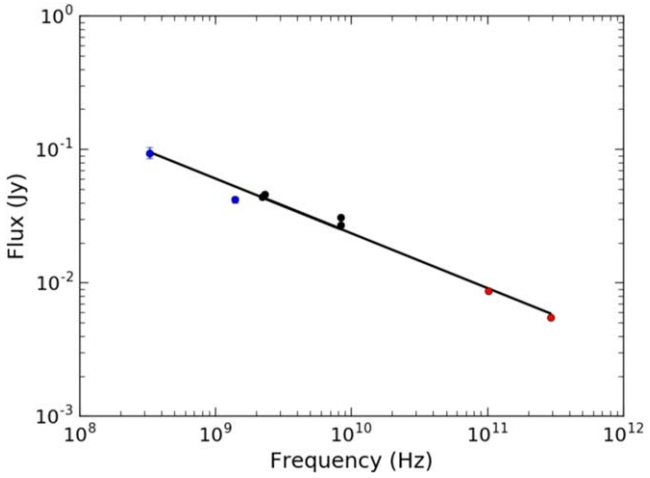

Figure 1. Radio to millimeter spectral energy distribution for the RXC J1504 BCG. The ALMA measurements are shown in red. A contribution from the radio minihalo has been removed to obtain the blue points (Giacintucci et al. 2011). The error bars for the blue and red points are shown, but they are smaller than the marker. No uncertainties are available for the black points.

was shifted by 0.″48 (N 30° E) in order to line up this galaxy with the submillimeter continuum.

The F165LP image contains no compact sources to compare to the F689m or ALMA images. However, the same filamentary structure appears in each image. The F165LP image was shifted manually by 1.″37 (W 5° S) in order to line up similar features in the two *HST* images. This shift is probably accurate to a few tenths of an arcsecond, although this is difficult to quantify. An 8° counterclockwise rotation was also applied to the F165LP image in order to better align the UV emission with the molecular filament seen in the CO (3–2) image. The choice of aligning each image with the ALMA images was arbitrary. Only relative distances are used in this work, so any systematic errors in absolute positions do not affect our results.

3. Results

3.1. AGN Continuum

Our ALMA observations of the continuum point source in RXC J1504 extend previous radio measurements to millimeter wavelengths. The spectral energy distribution is shown in Figure 1 and has been fit with a power law of the form $S \propto \nu^{-\alpha}$. The GMRT 327 MHz and VLA 1.4 GHz observations, shown in blue, both include emission from a radio minihalo. Giacintucci et al. (2011) isolated the contribution from the AGN by modeling the spatial distribution with a two-dimensional Gaussian. Error bars are included for both the blue (GMRT and VLA) and red (ALMA) points but are unavailable for the other VLBI measurements (black points: Bourda et al. 2010; Petrov 2013). The spectral index of the power law is $\alpha = 0.41 \pm 0.03$. This is a flat-spectrum source that is consistent with synchrotron emission from the AGN.

3.2. Integrated Spectra

The spatially integrated CO (1–0) and CO (3–2) spectra were extracted from a polygonal region tracing the significant CO (1–0) emission, which was determined from the maps presented in Section 3.4. The region measured ∼28 kpc along its long axis and 11.4 kpc in the orthogonal direction. The

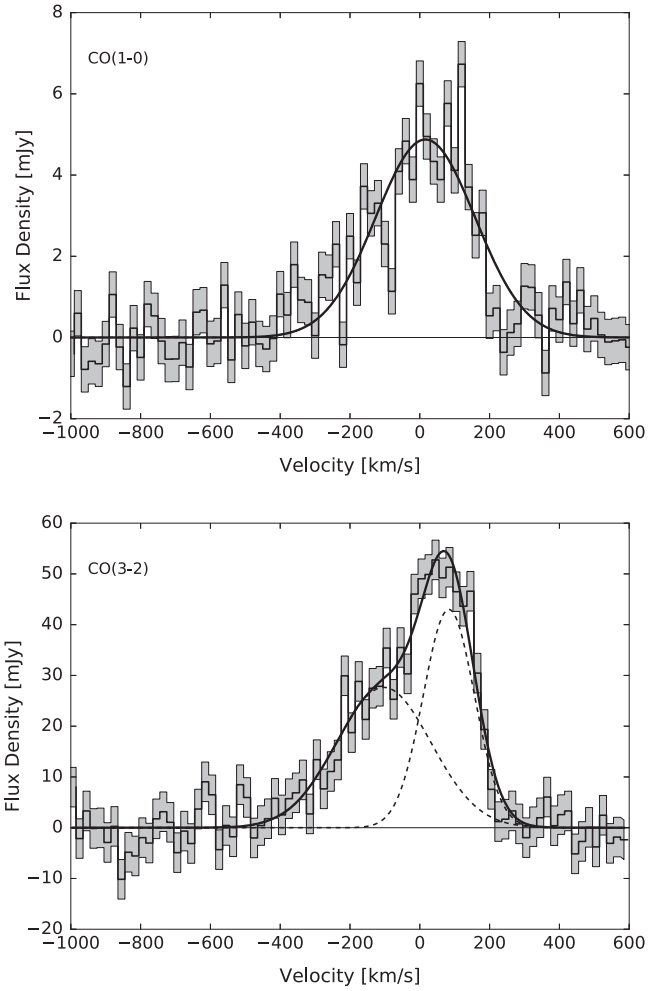

Figure 2. Spatially integrated CO (1–0) (top) and CO (3–2) (bottom) spectra. The shaded areas indicate the rms noise in line-free channels.

integrated CO (1–0) and CO (3–2) spectra are shown in Figure 2. The spectra have been corrected for the response of the primary beam.

All spectra throughout this work were fit by either one or two Gaussian components. The LMFIT package[10] was used to perform the spectral fitting. Each spectral component was tested using a Monte Carlo analysis with at least 1000 iterations, with a detection requiring a 3σ significance (see Section 5.2 of Protassov et al. 2002). The presence of one component was required before attempting to fit a second. Instrumental broadening has been incorporated into the model.

The spatially integrated CO (1–0) spectrum was best fit by a single component centered at 16.0 ± 6.5 km s^{-1} with an FWHM of 335 ± 15 km s^{-1} and integrated flux of 1.74 ± 0.07 Jy km s^{-1}. The higher signal-to-noise ratio in the CO (3–2) spectrum shows that the spatially integrated spectrum is better fit by two velocity components. The first component, with an integrated flux of 9.4 ± 3.1 Jy km s^{-1}, is centered at -103 ± 51 km s^{-1} with an FWHM of 319 ± 72 km s^{-1}. The other component is redshifted to 83.2 ± 7.9 km s^{-1} and has an FWHM of 173 ± 23 km s^{-1}. A list of the best-fitting parameters can be found in Table 1.

[10] https://lmfit.github.io/lmfit-py/

Table 1
Parameters of Molecular Features

Region	J_{up}	χ^2/dof	Velocity Center (km s^{-1})	FWHM (km s^{-1})	Integrated Flux[a] (Jy km s^{-1})	Gas Mass[a] ($10^8\,M_\odot$)	Integrated Flux[b] (Jy km s^{-1})	Gas Mass[b] ($10^8\,M_\odot$)
Integrated	1	223/97	16.0 ± 6.5	335 ± 15	1.74 ± 0.07	173 ± 7	1.90 ± 0.02	189 ± 2.5
	3	94/74	−103 ± 51	319 ± 72	9.4 ± 3.1	104 ± 34	17.2 ± 0.8	190 ± 9
			83.2 ± 7.9	173 ± 23	7.9 ± 3.0	87 ± 33	...	...
Central 5 kpc	3	225/154	−85 ± 13	362 ± 25	10.8 ± 0.8	119 ± 9	13.78 ± 0.67	152 ± 7
			127 ± 4	121 ± 13	3.35 ± 0.59	37.0 ± 6.5	...	...
Central clump	3	268/157	−48 ± 5	413 ± 12	11.68 ± 0.29	129 ± 3.2	11.38 ± 0.53	126 ± 6
NE clump	3	180/157	129.7 ± 2.6	116 ± 6	2.2 ± 0.1	24.3 ± 1.1	2.38 ± 0.35	26.3 ± 3.9
Nuclear clump	3	63/74	−164 ± 15	414 ± 21	6.02 ± 0.44	66.5 ± 4.9	7.10 ± 0.40	78.4 ± 4.4
			−30 ± 8	130 ± 26	1.17 ± 0.34	12.9 ± 3.8	...	...
Filament	3	250/74	−134 ± 11	123 ± 25	1.18 ± 0.24	13.0 ± 2.7	4.33 ± 0.65	48 ± 8
			37 ± 5	144 ± 12	3.33 ± 0.25	36.8 ± 2.8	...	...
Inner filament	3	202/157	−124.7 ± 3.4	101 ± 8	1.10 ± 0.08	12.1 ± 0.9	0.79 ± 0.28	8.7 ± 3.1
Middle filament	3	287/157	1.2 ± 2.7	82.2 ± 6.5	1.65 ± 0.11	18.2 ± 1.2	1.63 ± 0.46	18.0 ± 5.0
Outer filament	3	103/77	80.3 ± 4.2	94 ± 10	1.57 ± 0.14	17.3 ± 1.5	0.92 ± 0.48	10.2 ± 5.3

Notes. All spectra have been corrected for the response of the primary beam and instrumental broadening. Masses determined from the CO (3–2) line have been calculated assuming CO (3–2)/(1–0) = 9 (in flux units), determined from the spatially integrated spectra.
[a] Determined by the model fitting of one or two Gaussians.
[b] Determined by numerically integrating the spectrum.

Previous single-dish measurements of RXC J1504–0248 with the IRAM 30 m telescope recovered an integrated CO (1–0) flux of 3.84 ± 0.62 Jy km s^{-1} (Edge, unpublished). The integrated flux measured by ALMA is 45% ± 8% of this single-dish measurement. Similar recovered fractions were measured in RX J0821 (Vantyghem et al. 2016), NGC 5044 (David et al. 2014), and A1664 (Russell et al. 2014). Missing short spacings filter out emission on scales larger than 9.″2 at CO (1–0) and 6 arcsec at CO (3–2).

The ratio of integrated flux densities determined from the spatially integrated spectra is CO (3–2)/(1–0) = 9.0 ± 0.4 in flux units, or CO (3–2)/(1–0) = 1.00 ± 0.04 in intensity units. This is higher than the CO (3–2)/(1–0) ≈ 7 measured in other BCGs (e.g., Vantyghem et al. 2014, 2016; Russell et al. 2016). The equal CO (1–0) and CO (3–2) intensities indicate that the molecular clouds are thermalized. This is the case when the H_2 density exceeds the critical density for the transition, which is ∼700 cm^{-3} for CO (1–0) and ∼2 × 10^4 cm^{-3} for CO (3–2). The molecular gas in RXC J1504 therefore resides primarily in dense clouds, as opposed to a more diffuse, volume-filling phase.

In addition to model fitting with one or two Gaussians, we have also numerically integrated the spectra following the approach of Young et al. (2011). Briefly, integrated fluxes were computed by summing each spectrum over velocity. The uncertainty in the integrated flux, σ_F, is determined from

$$\sigma_F^2 = (\Delta v)^2 \sigma^2 N_l (1 + N_l/N_b). \quad (1)$$

Here, Δv is the velocity bin size, σ is the rms in line-free channels, N_l is the number of velocity bins, and N_b is the number of bins used to measure the baseline. Numerical integration is well suited to measuring the total integrated flux, particularly when multiple Gaussians are required to fit the spectrum. The fluxes in multicomponent spectra have large uncertainties due to degeneracies in fitting overlapping Gaussians. Adding these uncertainties in quadrature to determine the total flux is inappropriate, as the individual components are not independent. The total fluxes and masses quoted for multicomponent spectra throughout this work therefore adopt the values measured via numerical integration.

3.3. Molecular Gas Mass

The integrated flux ($S_{CO}\Delta v$) of the CO (1–0) line can be converted to molecular gas mass through (Solomon et al. 1987; Solomon & Vanden Bout 2005; Bolatto et al. 2013)

$$M_{mol} = 1.05 \times 10^4 \frac{X_{CO}}{X_{CO,gal}} \left(\frac{S_{CO}\Delta v\, D_L^2}{1+z} \right) M_\odot. \quad (2)$$

Here, z is the redshift of the source, D_L is the luminosity distance in Mpc, and $S_{CO}\Delta v$ is in Jy km s^{-1}. The CO-to-H_2 conversion factor, X_{CO}, is an empirically derived quantity that is poorly constrained in BCGs. Standard practice, which we have applied here, has been to adopt the Galactic value of $X_{CO,gal} = 2 \times 10^{20}$ cm^{-2}(K km s^{-1})$^{-1}$ (Bolatto et al. 2013).

Whether the Galactic X_{CO} is appropriate for BCGs is unknown. In the disks of normal, solar-metallicity galaxies, Bolatto et al. (2013) recommend adopting the Galactic conversion factor with a factor of two uncertainty. The metal abundances in the hot cluster atmospheres surrounding BCGs are typically ∼0.6–0.8 $Z_\odot$, which is high enough for the Galactic X_{CO} to be applicable. However, X_{CO} also depends on excitation conditions. The warm, dense gas in starbursts and (ultra)luminous infrared galaxies (U/LIRGs) results in a conversion factor roughly five times lower than Galactic. The SFR in RXC J1504–0248 (136 $M_\odot$ yr^{-1}; Ogrean et al. 2010) may be high enough to justify a LIRG-like X_{CO}.

Recently, the detection of a ^{13}CO line in the galaxy cluster RX J0821.0+0752 allowed X_{CO} to be estimated for the first time in a BCG (Vantyghem et al. 2017). This study obtained an X_{CO} that is a half of the Galactic value, albeit with large systematic uncertainties. We continue to follow the standard practice of adopting the Galactic X_{CO} until more direct calibrations in BCGs are available.

In order to compute molecular gas mass from a CO (3–2) flux, we first convert it to a CO (1–0) flux by adopting the

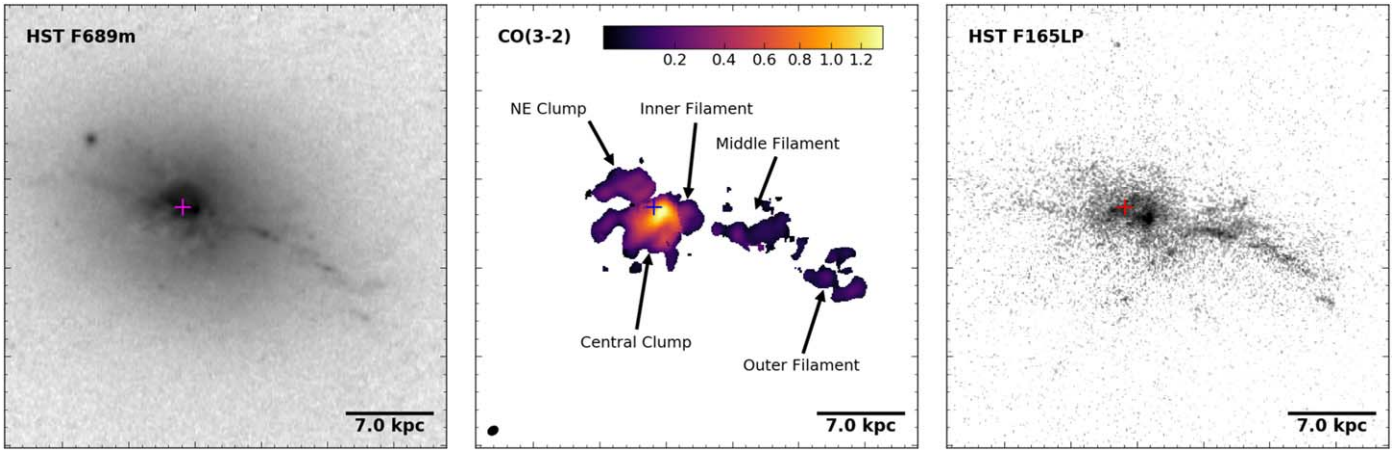

Figure 3. *HST* UVIS F689m (left), ALMA CO (3–2) (middle), and *HST* ACS F165LP (right) images showing the same 35 kpc × 35 kpc field of view. The color bar in the middle panel shows the CO (3–2) integrated flux in Jy km s^{-1}. The plus sign indicates the position of the nuclear submillimeter continuum source. The black ellipse in the lower left corner shows the size of the synthesized beam.

CO (3–2)/(1–0) line ratio of 9 measured from the spatially integrated spectra. From the integrated spectra presented in Section 3.2, the total molecular gas mass measured with the higher-fidelity CO (3–2) spectrum is $(1.9 \pm 0.1) \times 10^{10}\,M_{\odot}$.

3.4. Molecular Gas Distribution and Kinematics

Maps of integrated flux, velocity, and FWHM were created by applying the spectral fitting routine discussed in Section 3.2 to the spectra extracted from individual pixels, which were averaged over a box the size of the synthesized beam. A total of 2500 iterations were used for the Monte Carlo analysis, with a detection requiring 3σ significance. The CO (3–2) integrated flux map is shown alongside the *HST* UVIS F689m and ACS F165LP images in Figure 3. The location of the submillimeter continuum is indicated by the plus sign. The maps of velocity and FWHM are shown in Figure 4. The CO (1–0) maps are not shown because they are consistent with the CO (3–2) maps but have a lower resolution and sensitivity.

At the redshift of RX J1504, the F689m filter covers the wavelength range 5340–5960 Å. This range excludes both the [O III]/Hβ and [N II]/Hα emission line complexes. As a result, only the continuum emission from old and young stars is present in Figure 3 (left). Similarly, the F165LP filter is sensitive to far-UV (FUV) photons, tracing the young stellar population. The filamentary emission observed in the optical (Figure 3, left) is also seen in the ultraviolet, indicating that this emission stems from young stars.

The molecular gas distribution is complex and disturbed. The CO line emission peaks 0.8 kpc away from the submillimeter continuum source. Nearly 80% of the molecular gas is located within 5 kpc of the galactic center. This region comprises a large, central clump and a smaller clump to the NE. Beyond this region, a clumpy, 20 kpc long filament extends radially from the galactic center. It is coincident with continuum emission from the young stellar population observed in both *HST* images. Spectral fits for these regions, as well as others discussed below, are provided in Table 1.

These morphological features are composed of at least three distinct velocity components. The first is redshifted emission from the NE clump and a portion of the large, central clump. Next, the filament extends from a galactocentric distance of 20 kpc all the way into the central clump, with a smooth velocity gradient throughout. Finally, a broad, blueshifted clump is coincident with the submillimeter continuum source. The filament and blueshifted clump have been grouped together in the right panels of Figure 4, while the remaining emission is shown on the left. Two velocity components were required to fit the spectra of gas in the immediate vicinity of the submillimeter continuum source.

The NE clump and much of the central clump are part of the same kinematic structure. These regions share a common line-of-sight velocity, reaching a maximum of 150 km s^{-1}. Toward the galactic center the velocity transitions sharply from 60 to -40 km s^{-1} over a distance of 1 kpc, which is about four resolution elements. Closest to the AGN, where multicomponent emission is detected, the redshifted component is moving close to the systemic velocity. The line widths throughout the emission east of the BCG nucleus vary between 70 and 150 km s^{-1}. The narrowest regions tend to be farthest from the nucleus, although no clear gradients in the line width are present.

The filament exhibits a smooth velocity gradient, ranging from -110 km s^{-1} near the cluster core to 150 km s^{-1} at a radius of 20 kpc. The line widths along the filament are narrow, ranging from 30 to 100 km s^{-1} without a clear radial dependence. These line widths are comparable to those in the filaments observed in other systems (e.g., Russell et al. 2016; Vantyghem et al. 2016). The filament is clumpy. In addition to the two clumps visible in the integrated flux map shown in Figure 3, a third clump forms part of the large central clump. It is distinguished as part of the filament by its velocity and line width. The blueshifted velocity connects smoothly to the middle portion of the filament, while the line width is consistent with that at larger radii. A region outlining the full extent of the filament is shown in the bottom right panel of Figure 4. Individual spectral fits for this region and each of the three smaller clumps within it are provided in Table 1. The total molecular gas mass in the filament is $4.8 \times 10^{9}\,M_{\odot}$, with the three clumps each having comparable masses.

The nuclear gas in the right panels of Figure 4 is marked by a sharp jump in both velocity centroid and line width. The innermost velocity in the filament is -110 km s^{-1}, while the gas coincident with the submillimeter continuum has a velocity of -180 km s^{-1}. A more drastic change is seen in the line width, which changes abruptly from 110 km s^{-1} in the filament

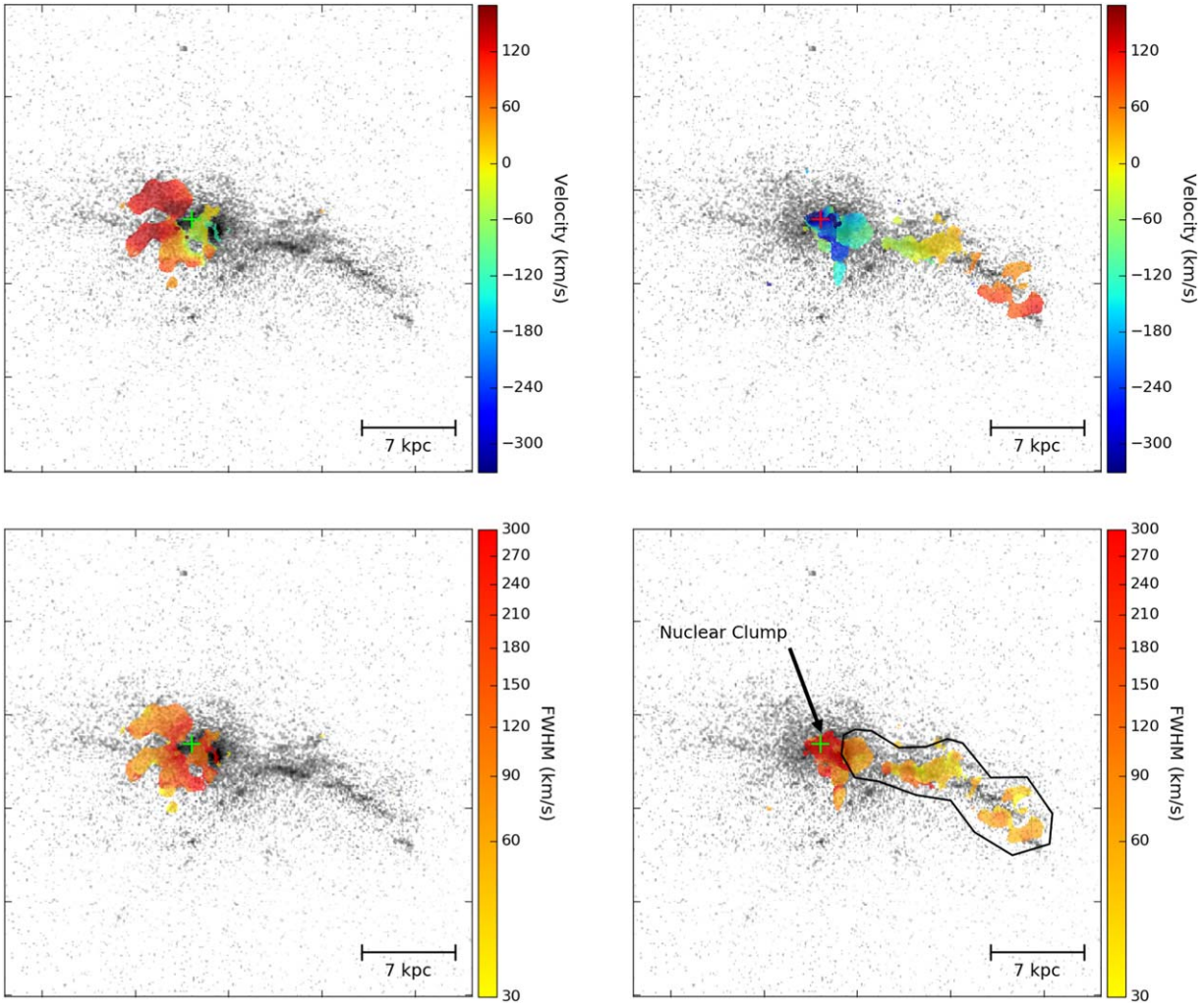

Figure 4. Maps of velocity centroid (top) and FWHM (bottom) overlaid on the *HST* ACS F165LP image. The emission from the filament and the broad, nuclear component were isolated in the right panels. The remaining emission, consisting of the redshifted clump to the NE and some central gas near the systemic velocity, is shown on the left. Two velocity components are present near the continuum source, which is indicated by the plus sign. The full extent of the filament, which extends into the central clump, is outlined in the bottom right panel.

to 300 km s^{-1} at the nucleus. As a result, we consider the nuclear gas to be dynamically distinct from the filament.

Alternatively, the sharp change in velocity can be attributed to the presence of a second velocity component coincident with the nucleus. If the filament hosted two velocity components, one of which was not being detected significantly, then the best-fitting model would have a moderate central velocity. When the faint component becomes significant, the best-fitting model will have two peaks: one more blueshifted and one more redshifted than the single-component model. This will result in an apparent jump in velocity at the interface between one- and two-component regions. This interface would also exhibit a decrease in line width, as the two components are each narrower than a single-component fit to the spectrum. However, the velocity jump seen toward the cluster core shows a significant *increase* in line width. The second velocity component also smoothly connects to the redshifted emission on the other side of the galaxy, so it is likely unrelated to the filament. Thus, the central clump does not connect smoothly in phase space to the adjacent filament.

As discussed in Section 3.2, the total molecular gas mass determined from the CO (3–2) spectrum is $(1.9 \pm 0.1) \times 10^{10}\,M_{\odot}$. The gas within the central 5 kpc, which includes both the central and NE clumps, accounts for 80% ($1.5 \times 10^{10}\,M_{\odot}$) of the total mass. Most of this gas is concentrated within the central clump, with only 16% ($2.6 \times 10^{9}\,M_{\odot}$) located in the NE clump. The remaining 20% of molecular gas is contained within the middle and outer clumps of the filament. After including the contribution coming from the component within the central clump, the total filament mass is $4.8 \times 10^{9}\,M_{\odot}$, or about 25% of the total gas mass. The mass of the nuclear, blueshifted clump is best estimated from a fairly restrictive (3.5×2.6 kpc) region encompassing only the nuclear emission. A multicomponent fit yields a total mass for the broad component of $6.5 \times 10^{9}\,M_{\odot}$. This is 40% of the central clump and 35% of the total gas mass. The mass of the redshifted kinematic component is complicated by overlapping contributions from the broad component and inner filaments that make up the central clump. Removing these contributions yields a total mass of $7.2 \times 10^{9}\,M_{\odot}$ for the redshifted structure.

Hosting both blueshifted and redshifted emission, the nuclear velocity structure could be interpreted as rotation. The filament, whose velocity gradient has the opposite sign, is dynamically distinct from the nuclear gas. However, the

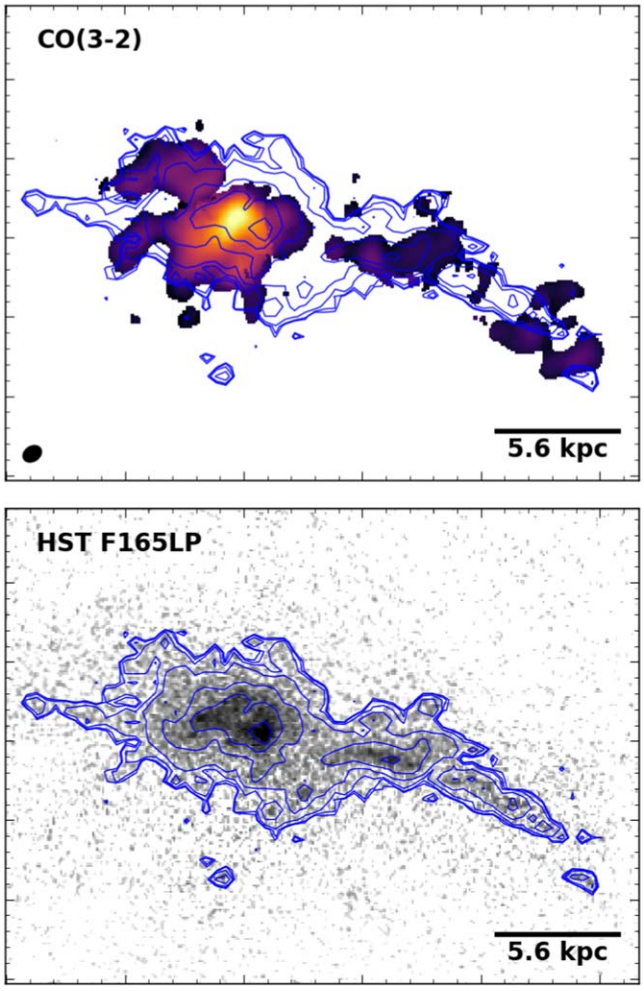

Figure 5. ALMA CO (3–2) (top) and *HST* F165LP (UV; bottom) images that were shown in Figure 3, but overlaid with contours of the UV emission.

morphology of the nuclear gas does not resemble a rotationally supported equilibrium structure, such as a disk. An equilibrium structure should straddle the gravitational center. Instead, the blueshifted emission is exclusively coincident with the nucleus, while the redshifted emission extends to both the NE and SE. Any resolved equilibrium structure would need to be in the early stages of formation. The line width of the blueshifted emission also differs significantly from the redshifted gas, indicating that it is not part of a common structure.

The broad line width of the gas coincident with the continuum point source may indicate that it has settled within the underlying potential. If it is an unresolved disk, then it must be <1.2 kpc in diameter, much smaller than the 7 kpc disk observed in Hydra A (Hamer et al. 2014). However, the velocity of this component is ~ -250 km s^{-1}, making it the most blueshifted gas in the system. Since this would also be located at the kinematic center of the BCG, all of the remaining gas would be redshifted in comparison. This is unlikely to be the case. If the gas has only recently formed, then the entirely redshifted emission implies a highly asymmetric origin of the cold gas. Alternatively, if some of the gas has survived for longer than a dynamical time, the gas velocities should have begun to center on the systemic velocity of the BCG, and by extension the nuclear disk.

3.5. Spatial Correlation with UV Emission

In Figure 5 we present a direct comparison between the CO (3–2) emission and UV continuum. The distributions of molecular gas and young stars are qualitatively similar on large scales. Both are brightest near the galactic center and contain a filament extending to the SW.

It is important to note that the *HST* F165LP image was shifted manually in order to align the UV and CO emission both in the center and along the filament. Spatial offsets between the molecular gas and young stars could be present but would be missed owing to this manual alignment. However, the UV and CO morphologies agree relatively well. Additional shifting of the UV emission to better line up certain features would generally degrade the correlation between other structures.

For this reason comparisons on smaller scales should be taken with caution. Nevertheless, we note that the molecular gas and star formation in the outer portions of the filament are possibly anticorrelated. The three clumps within the outer filament are not coincident with enhanced UV emission. Instead, a clump of UV emission lies just beyond the outermost molecular clump. Similarly, UV emission connects the middle and outer molecular clumps, passing in between two of the molecular clumps in the outer filament. This anticorrelation may indicate that active star formation along the filament has already churned through the local gas supply.

4. Discussion

4.1. Gas Origin

The massive molecular gas reservoirs in BCGs are strongly linked to condensation from the hot atmosphere. Most directly, molecular gas and star formation are only present in clusters where the central cooling times fall below $\sim$1 Gyr (Rafferty et al. 2008; Pulido et al. 2017). Rates of mass condensation in the hot atmosphere are also correlated with the SFR of the BCG (O'Dea et al. 2008). Both of these correlations indicate that the presence of molecular gas in a central cluster galaxy depends on the atmospheric properties of its host cluster.

Alternative supplies of molecular gas include minor mergers and stripping. The frequency of minor mergers and the efficiency of tidal stripping are not affected by the presence of a cool core. Moreover, roughly 85% of elliptical galaxies have $<10^8\,M_\odot$ of molecular gas (Young et al. 2011). Accumulating $10^{10}\,M_\odot$ of cold gas, as observed in several systems, would take hundreds to thousands of mergers. Ram pressure stripping, on the other hand, is potentially linked to the presence of cool cores because it is more efficient in their dense cores. However, small spirals will be stripped well outside of the central galaxy, and high-mass systems (LIRGs, ULIRGs) will remain bound (Kirkpatrick et al. 2009). Large spiral galaxies on nearly radial trajectories will deposit their gas within the central 10 kpc, but these are rare, and each galaxy should only contribute a few $\times\,10^8\,M_\odot$ of molecular gas. As a result, minor mergers, tidal stripping, and ram pressure stripping are all unlikely to be viable mechanisms for supplying the rich reservoir of cold gas in BCGs.

RXC J1504 has one of the most extreme cooling cores ever discovered. Its hot atmosphere is condensing at a rate of $\sim 80\,M_\odot$ yr^{-1} (Ogrean et al. 2010), which can supply its $1.9\times10^{10}\,M_\odot$ of molecular gas in 2.4×10^8 yr. This is well matched to both the central cooling time, 2.3×10^8 yr, and the

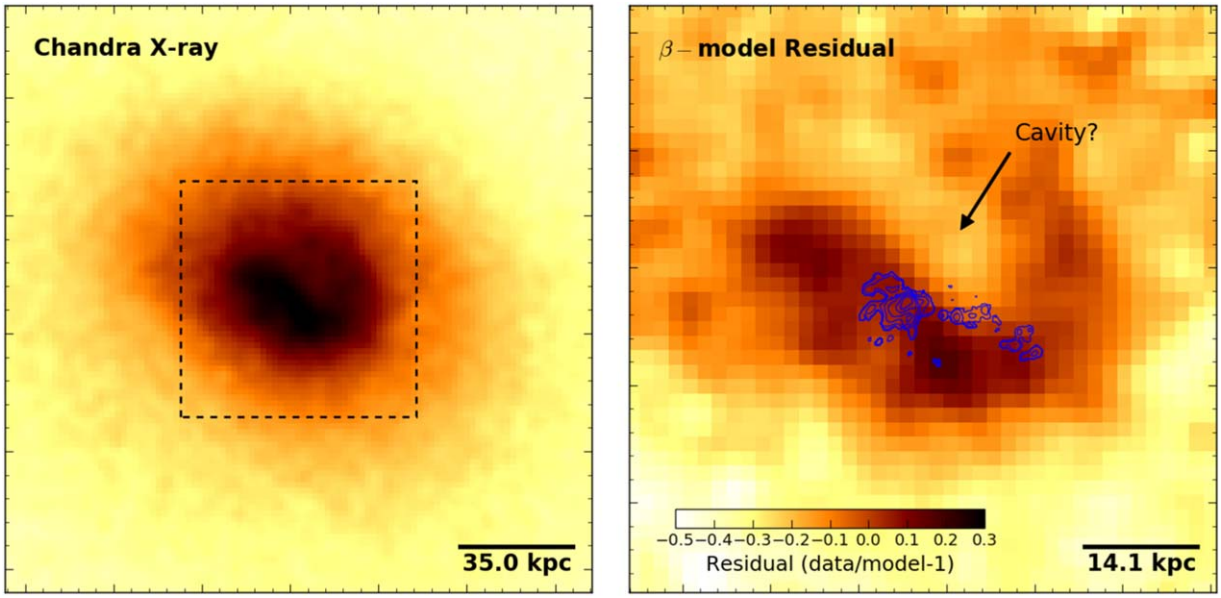

Figure 6. Left: *Chandra* X-ray image in the 0.5–7 keV band. The dashed box indicates the field of view for the right panel. Right: residual X-ray surface brightness after subtracting a double β-model. Contours of the CO (3–2) emission are overlaid.

timescale to be consumed by star formation, 1.4×10^8 yr (see Section 4.3). The total amount of hot gas within the central 15 kpc, $4 \times 10^{10}\,M_\odot$, also exceeds the total molecular gas mass. Condensation of the hot atmosphere can therefore fuel the production of molecular gas.

Here we explore the potential triggers that could result in the formation of the molecular filament. These processes must produce nonlinear density perturbations in the cluster atmosphere, which then become thermally unstable and condense into the observed molecular gas (Pizzolato & Soker 2005, 2010).

A *Chandra* X-ray image of the cluster from a combined 160 ks exposure (observation IDs 4935, 5793, 17197, 17669, and 17670) is shown in Figure 6. The X-ray surface brightness profile was extracted from elliptical annuli centered on the optical centroid of the BCG with 2.″5 (8.8 kpc) widths along their major axis. The axis ratio (1.2) and position angle (53° east of north) were determined qualitatively. The profile was well fit by a double-β model (Cavaliere & Fusco-Femiano 1976), which was then subtracted from the original image to produce the residual map in the right panel of Figure 6. Contours of the CO (3–2) emission are overlaid on this image.

A positive residual straddles the central clump of molecular gas. It is oriented from NE to SW and contains two bright peaks located about 10 kpc from the BCG nucleus. The positive residual curves northward at the SW tail of this filament, forming an arc that is associated with what could be an X-ray cavity, as indicated in the right panel of Figure 6. The residual image reproduces the sloshing fronts identified in a single 40 ks *Chandra* exposure (Giacintucci et al. 2011). The southern front is demarcated by the sharp drop in X-ray surface brightness in the lower left area of the right panel of Figure 6. The northwestern edge is located just outside of the field of view of the residual image. The cavity was not detected in the previous *Chandra* analysis, likely due to the lower signal-to-noise ratio that was available.

The feature identified as a potential cavity is poorly defined, so it is not clear whether it is a real cavity. Archival observations of the radio continuum are low resolution and so cannot be used to identify any synchrotron emission originating within the surface brightness depression. However, X-ray cavities are nearly ubiquitous in cool core clusters. At least 70% of the clusters in the Brightest 55 sample host radio bubbles (Dunn et al. 2005). Accounting for the presence of cavities that are undetected owing to projection effects can boost this fraction to ∼100% (Bîrzan et al. 2012). Since RXC J1504 is one of the most extreme cooling cores known, it is likely that it hosts AGN activity. In addition, an analysis of a volume-limited sample showed that all sources with at least 30,000 X-ray counts within the central 20 kpc have clearly detected cavities (Panagoulia et al. 2014). The central 20 kpc of RXC J1504 contains 40,000 X-ray counts, suggesting that the identified surface brightness depression is a real cavity.

If the identified feature does correspond to a real cavity, then its projected size is approximately 10×7 kpc. At a projected distance of 10 kpc from the BCG nucleus, the gas temperature, density, and pressure are 4.57 keV, 0.15 cm^{-3}, and 2×10^{-9} erg cm^{-3}, respectively. The corresponding cavity enthalpy, buoyancy time, and jet power are 5.6×10^{59} erg, 20 Myr, and 9.1×10^{44} erg s^{-1}, respectively. These properties were calculated following the standard analysis (see, e.g., Bîrzan et al. 2004; Rafferty et al. 2006; Vantyghem et al. 2014). Note that the gravitational acceleration used to compute the buoyancy time was determined from the Hernquist profile in Section 4.2, as the cavity is sufficiently close to the BCG nucleus.

For comparison, the cavity power can also be estimated from the scaling relation (Cavagnolo et al. 2010)

$$\log P_{\mathrm{cav}} = 0.75(\pm 0.14)\log P_{1.4} + 1.91(\pm 0.18). \quad (3)$$

Here, P_{cav} is in units of 10^{42} erg s^{-1} and $P_{1.4}$, the radio power at 1.4 GHz, is in units of 10^{40} erg s^{-1}. The RXC J1504 BCG contains a 42 mJy point source at 1.4 GHz (Bauer et al. 2000; Giacintucci et al. 2011). The corresponding 1.4 GHz luminosity is 5.8×10^{24} W Hz^{-1} , and the power is 8×10^{40} erg s^{-1}. The scaling relation then yields a cavity power of

$(3.9 \pm 2.0) \times 10^{44}$ erg s^{-1}. This is 2.5σ smaller than the cavity power derived from the X-ray observation.

4.1.1. Merger

While repeated minor mergers with donor galaxies are unable to supply the molecular gas themselves, the passage of a galaxy through the cluster core may perturb the hot atmosphere enough to instigate condensation. Several small galaxies are situated along the axis of the filament, the closest of which is 25 kpc east of the BCG. This galaxy is moving at approximately 65 km s^{-1} with respect to the BCG, so it is a cluster member and could have interacted with the BCG in the past. However, the molecular gas extends only 5 kpc east of the BCG nucleus. Either the cluster atmosphere immediately trailing the galaxy has not had time to condense, or this galaxy is unrelated to the molecular gas. The latter is more likely. Galaxies pass through cluster cores only rarely, so the high fraction of gas-rich BCGs in cool core clusters is likely unrelated to the motion of the member galaxies. Additionally, the molecular gas distributions in other cool core clusters observed by ALMA were not explained by perturbations caused by member galaxies. A merger-induced formation process for the molecular gas is unlikely.

4.1.2. Stimulated Cooling

Previous ALMA observations of BCGs have revealed molecular filaments that are exclusively oriented toward X-ray cavities (e.g., McNamara et al. 2014; Russell et al. 2016, 2017; Vantyghem et al. 2016). The velocities along these filaments lie below the terminal velocity of a rising bubble, indicating that the filaments may be caught in the updraft of the buoyantly rising bubble. The cold gas either is lifted directly from a reservoir at the center of the BCG or has condensed in situ from the ICM that has been uplifted. In the "stimulated cooling" conjecture, low-entropy gas from the cluster core is lifted by a radio bubble to a radius where its cooling time is shorter than the time required to fall to its equilibrium position (McNamara et al. 2016). The low velocities observed in molecular filaments indicate that this infall time, t_I, is longer than the freefall time. A thermal instability would then ensue when $t_{\rm cool}/t_I \lesssim 1$.

The molecular gas in RXC J1504 is mostly confined to the central 5 kpc, with a filament extending 20 kpc to the WSW. The velocity gradient along the filament resembles those oriented behind X-ray cavities in other systems. As seen in the right panel of Figure 6, the molecular filament is associated with both the putative X-ray cavity and a region of enhanced X-ray emission. Other BCGs also exhibit a spatial correlation between molecular and X-ray filaments (e.g., Vantyghem et al. 2016). However, those filaments generally trail directly behind X-ray cavities, which is not the case in RXC J1504. Instead, the cavity is located very close to the cluster core, and the filament extends along its inner edge.

The poor spatial correlation between the filament and the cavity may be indicative of complex hot phase dynamics within the cluster core. Giacintucci et al. (2011) identified two cold fronts that were likely created by the sloshing of the cool core. This suggests that the BCG is in motion with respect to the cluster potential. The combination of sloshing and continued AGN activity could stir the hot atmosphere in the cluster core. Nonlinear overdensities developed in this medium would not necessarily trail directly behind the cavity.

The maximum amount of gas that can be lifted by a cavity is limited by the amount of gas that it has displaced. The mass of hot gas that has been displaced by the putative cavity is $M_{\rm disp} = 2\mu m_p n_e V \approx 10^{10}\,M_\odot$, where n_e is the gas density, V is the cavity volume, m_p is the proton mass, and $\mu = 0.62$. The factor of two accounts for protons and electrons (i.e., $n = n_e + n_p$). Since the total molecular gas mass within the filament is $4.8 \times 10^9\,M_\odot$, the cavity could have lifted enough low-entropy gas to form the filament. This requires an efficient coupling between the cavity and filament, but a similar efficiency is measured in other BCGs (e.g., McNamara et al. 2014; Russell et al. 2017). Its proximity to the cluster core also suggests that the cavity may still be influencing the dynamics of the filament. The filament is not purely radial. The middle portion is situated along the inner edge of the cavity, bending toward the SW at higher altitudes. The nonradial directionality of the filament may therefore arise because the inner portion of the filament is caught in an updraft behind the cavity.

As discussed in Section 4.1, gas condensation out of the hot atmosphere would take 2.4×10^8 yr to form the total molecular gas supply. The putative cavity is likely only involved in stimulating the production of the filament, with the central gas originating from an older cycle of cooling. Forming the filament alone, which accounts for about 25% of the molecular gas mass, would take 60 Myr. This is several times longer than the age of the putative cavity, estimated by its buoyant rise time to be 20 Myr. The AGN outburst therefore does not have enough time to stimulate the formation of the filament through purely radiative cooling. Interpenetration of hot particles into molecular clouds can lead to nonradiative cooling, alleviating this tension (Fabian et al. 2011). This process powers the nebular emission (Ferland et al. 2009), heating the cold gas and cooling the hot gas.

Overall, the case for stimulated cooling is weaker in RXC J1504 than in several other BCGs. Nevertheless, the cluster core exhibits the AGN activity that is expected to uplift low-entropy gas. Sloshing motions can also promote thermally unstable cooling. Much like uplift, they displace the central, low-entropy gas to larger altitudes.

4.2. Motion along the Filament

Gravitational infall and outflows generated by AGN activity are both plausible explanations for the smooth velocity gradient along the filament. Infall is perhaps the most natural explanation, as molecular clouds condensing from the surrounding hot atmosphere should then rain back onto the central galaxy. On the other hand, it is the gas that has been uplifted by X-ray cavities that is expected to become thermally unstable. Recently formed clouds should trace the velocity of the uplifted gas and so should initially be outflowing.

A clump reaches its terminal velocity, v_T, when the ram pressure of the medium it moves through balances its weight:

$$\rho_0 v_T^2 A = \Delta\rho V g. \tag{4}$$

Here, ρ_0 is the density of the surrounding medium, $\Delta\rho = \rho - \rho_0$ is the excess density in the clump, A and V are the effective area and volume of the clump, respectively, and $g = v_K^2/R$ is the gravitational acceleration. Writing $V/A \approx r$

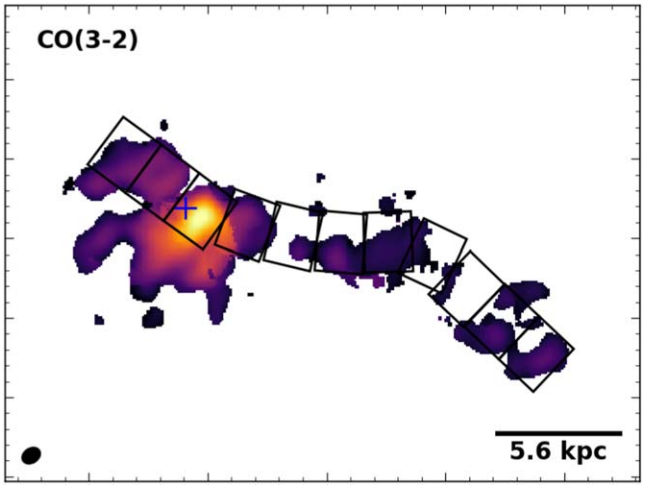

Figure 7. Regions used to extract the position–velocity diagram overlaid on the integrated CO (3–2) map.

as the approximate size of the clump and rearranging yields

$$\frac{v_T}{v_K} = \sqrt{\left(\frac{\rho}{\rho_0} - 1\right)\frac{r}{R}}. \quad (5)$$

If $v_T \geqslant v_K$, then the clump will be in freefall, as it never reaches its terminal speed.

The outer filament is composed of three distinct clumps. Each clump contains approximately 1/3 of the total molecular gas mass in the outer filament, so we take $M_{\rm mol} = 5.7 \times 10^8\, M_\odot$ for a single one of these clumps. The outermost clump is located $R = 16.8$ kpc from the BCG nucleus and is ≈1.4 kpc in radius. Conservatively assuming that the molecular gas mass fills its entire volume, the mean clump density is 4×10^{-24} g cm^{-3}. At a radius of 16.8 kpc the mean ambient density is 0.14 cm^{-3}, corresponding to a mass density of $\rho_0 = 2\mu m_p n_e = 3 \times 10^{-25}$ g cm^{-3}. This yields a terminal velocity $v_T \approx v_K$. The outermost clump should therefore be experiencing freefall.

Repeating this calculation for the middle filament similarly suggests that the molecular clouds should be in freefall. The total molecular gas mass within the middle filament is $1.8 \times 10^9\, M_\odot$. The dimensions of this region measure 4.9 kpc × 2.5 kpc. We assume that the projected length is the same as the width of the filament, 2.5 kpc. At a radius of $R = 10$ kpc the ambient density is 0.156 cm^{-3}. The resulting terminal speed is $v_T \approx 1.25 v_K$. Real molecular clouds are likely smaller and much denser than we have assumed here. The terminal velocities of these clouds would be even larger than we have calculated. The molecular gas in RXC J1504 should therefore be decoupled from the hot atmosphere, with only gravity dictating its acceleration.

A position–velocity diagram was extracted from the CO (3–2) image using the Python package PVExtractor. The path used to extract the spectra traced the entire length of the filament, passing through the center and extending to the NE clump. Spectra were extracted in 0.″6 (2.1 kpc) intervals along this path, each with a width of 0.″75 (2.6 kpc). The regions are shown in Figure 7. The spectra were modeled in the same way as described in Section 3.2. Position–velocity and position–FWHM curves are shown in Figure 8. Positive distances are in the direction of the filament. The central region was best fit by two velocity components. To distinguish

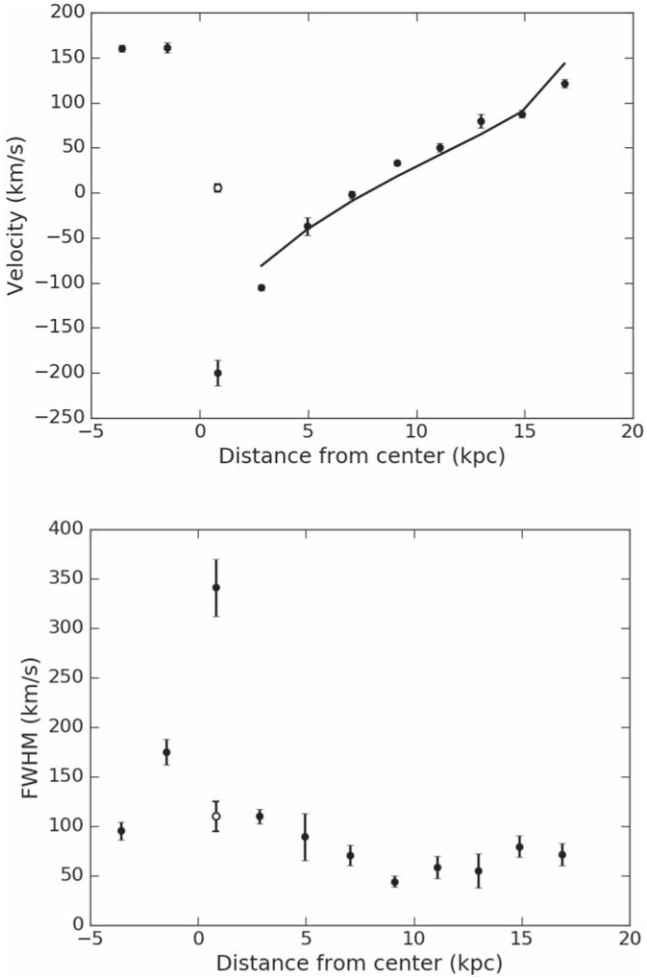

Figure 8. Position–velocity and position–FWHM curves extracted from a 0.″75-wide line segment tracing the filament and extending to the redshifted clump NE of center. The positions run from NE to SW, with positive distances corresponding to SW of center. The open circle indicates a second velocity component within a region. Various models of infall were fit to the points corresponding to the filament, as described in the text.

the second component between the two panels, it has been plotted as an open circle.

The position–velocity curve clearly shows the smooth velocity gradient along the filament ($d \gtrsim 2$ kpc). Over the length of the filament the FWHM varies from 45 to 110 km s^{-1}, with regions closer to the nucleus exhibiting broader line widths. In the central region, which was fit with two velocity components, the velocity of one component appears to connect smoothly to the velocity profile of the filament. However, the FWHM of this component is much broader than the gas in the filament. For this reason we exclude the central region when referring to the filament. NE of the center (negative distances), the velocity is constant at ∼160 km s^{-1}, while the FWHM is larger closer to the nucleus.

The velocity along the filament varies smoothly from −105 km s^{-1} near the nucleus to 120 km s^{-1} at its farthest extent. With a total projected length of 14 kpc, the velocity gradient is 16 km s^{-1} kpc^{-1}. The mass flow rate can be approximated by assuming that the filament was initially a point mass that has stretched as the gas flows toward the galactic center. The inner and outer portions of the filament are moving apart at a speed Δv, which is the peak-to-peak velocity

change along the filament. The mass flow rate is then

$$\frac{\dot{M}_{\rm flow}}{M_\odot\ {\rm yr}^{-1}} = \left(\frac{M_{\rm fil}}{10^9\ M_\odot}\right)\left(\frac{\Delta v}{{\rm km\ s}^{-1}}\right)\left(\frac{L_{\rm fil}}{\rm kpc}\right)^{-1}, \quad (6)$$

where $M_{\rm fil}$ and $L_{\rm fil}$ are the mass and length of the filament, respectively. From the masses tabulated in Table 1, the total filament mass is $4.8 \times 10^9\ M_\odot$. From Equation (6) we estimate a mass flow rate of $75\ M_\odot\ {\rm yr}^{-1}$.

To test models of gravitational infall, the stellar mass of the BCG was first measured following the prescription of Hogan et al. (2017). We adopted the Two Micron All Sky Survey K-band magnitude K_{20}, which is defined at a radius ($r_{K,20}$) within which the mean brightness is 20 mag arcsec^{-2}. This magnitude was corrected for galactic extinction (Schlafly & Finkbeiner 2011), as well as evolution and the K-correction (Poggianti 1997). The stellar mass within $r_{K,20}$ (24.6 kpc) was then determined from (Bell et al. 2003)

$$\log\frac{M}{L_K} = -0.206 + 0.135\,(B - V). \quad (7)$$

With a $B - V$ color of 0.45 (Véron-Cetty & Véron 2010) and $K_{20,\rm corr} = 13.786$, the total stellar mass is $5 \times 10^{11}\ M_\odot$.

For our models of gravitational infall, we assume that the molecular clouds in the filament are in freefall within the gravitational potential of the BCG. Describing the BCG with a Hernquist profile (Hernquist 1990), the velocity of a cloud dropped from radius r_0 is given by

$$v(r)^2 = v(r_0)^2 + 2GM\left(\frac{1}{r+a} - \frac{1}{r_0+a}\right). \quad (8)$$

Here, M is the total stellar mass of the BCG and $a = 5.2$ kpc is a scale factor determined from the galaxy's half-light radius ($R_e \approx 1.8153a$). For a hydrostatic atmosphere a condensing cloud should initially be at rest with respect to the ICM, so we take $v(r_0) = 0$. Similarly, initially outflowing gas will eventually slow and come to rest before falling back onto the BCG. Accounting for the inclination of the filament (i) with respect to the plane of the sky and a bulk offset between the BCG and ICM ($v_{\rm ICM}$), the expected line-of-sight velocity is

$$v_{\rm obs}(r) = v(r)\sin i + v_{\rm ICM}. \quad (9)$$

The velocity profile of the filament is fitted with this expression. $v_{\rm ICM}$ and i are allowed to vary, while r_0 is fixed to the maximum radial extent of the filament (17.5 kpc).

The best-fitting velocity profile is overlaid on the position–velocity diagram in Figure 8. Dropping a molecular cloud from $r_0 = 17.5$ kpc requires an inclination angle of $-22°$ with a bulk offset of $v_{\rm ICM} = 140$ km s^{-1}. This model underestimates the slope of the velocity profile and would likely provide a very poor prediction at any extrapolated distances. Allowing r_0 to vary provides a better fit to the velocity profile but requires an $r_0 \approx 50$ kpc, which is roughly double the maximum extent of the nebular line emission (Ogrean et al. 2010). Thus, this simplistic infall model implies that if the gas along the filament is in freefall, it must lie within $\sim 20°$ of the plane of the sky.

The BCG luminosity used in this analysis has been truncated at $r_{K,20}$, so the corresponding mass likely underestimates the total stellar mass. An increase in M is degenerate with a decrease in the magnitude of the inclination angle. The filament would then be located even closer to the plane of the sky. Using a singular isothermal sphere instead of a Hernquist profile eliminates the dependency on $r_{K,20}$, as the ratio M/r that defines the potential is a constant. The best-fitting velocity profile for this potential is indistinguishable from the Hernquist profile, also requiring the same inclination angle (for fixed r_0).

The requirement that molecular filaments in freefall must lie close to the plane of the sky is unsettlingly common in BCGs. In virtually all BCGs observed with ALMA, the line width of the ensemble molecular gas distribution lies well below the stellar velocity dispersion. Where molecular filaments have been detected, the inclination angles are comparable to those measured here (e.g., Lim et al. 2008; Russell et al. 2016, 2017; Vantyghem et al. 2016). Moreover, the filaments in several systems do not exhibit velocity gradients, indicating that they are dynamically young and are not currently raining back onto the central galaxy (e.g., Gendron-Marsolais et al. 2018; G. R. Tremblay et al. 2018, in preparation). The paucity of high-velocity gas suggests that, despite their high densities, the molecular clouds in BCGs are not in freefall.

High-resolution X-ray spectroscopy of the Perseus Cluster obtained by *Hitomi* also suggests that molecular clouds are not freefalling. The velocities of the molecular gas are consistent with the bulk shear measured in the hot atmosphere, suggesting that the molecular gas moves together with the hot atmosphere (Hitomi Collaboration et al. 2016). Ram pressure therefore still plays a role in dictating the motion of molecular clouds. This result is also found in simulations, which measure line widths that are consistent with observations (e.g., Prasad et al. 2015; Li et al. 2017; Gaspari et al. 2018).

Several factors can alleviate the tension between our simple terminal velocity model and the apparent lack of freefalling clouds in both observations and simulations. First, the average cloud densities may be lower than is implied by the molecular gas alone. The correlation between molecular gas and soft X-ray emission (e.g., Fabian et al. 2006) suggests that molecular gas may be encased by a warm–hot envelope of lower-density gas, potentially tethered together by magnetic fields (Fabian et al. 2008; Russell et al. 2016). This would reduce the mean cloud densities and increase their cross section, making them more susceptible to ram pressure. Our model also assumes that the ICM is at rest with respect to the BCG. An AGN-driven wind would counteract the motion of the molecular clouds, increasing the ram pressure exerted on the clouds by increasing their relative velocity.

Both of these effects were explored analytically by Li et al. (2018), using the filaments in the Perseus Cluster (Fabian et al. 2008) as a test case. Without any modifications, the filament density of $n = 2\ {\rm cm}^{-3}$ would result in a terminal velocity of $\sim$1000 km s^{-1}, well above the observed velocities. Reducing the cloud density by a factor of 3 and introducing an AGN-driven wind brings the predicted velocities into agreement with observations. Thus, although the cloud densities in RXC J1504 imply that they should be moving ballistically, the presence of both a warm–hot envelope and an AGN-driven wind can reduce the terminal velocity significantly.

4.3. Star Formation along the Filament

The total extinction-corrected SFR within the central galaxy was measured using near-UV *GALEX* observations (rest-frame FUV) to be $136\ M_\odot\ {\rm yr}^{-1}$ (Ogrean et al. 2010). Applying the correction for the UV upturn used in the CLASH BCG sample

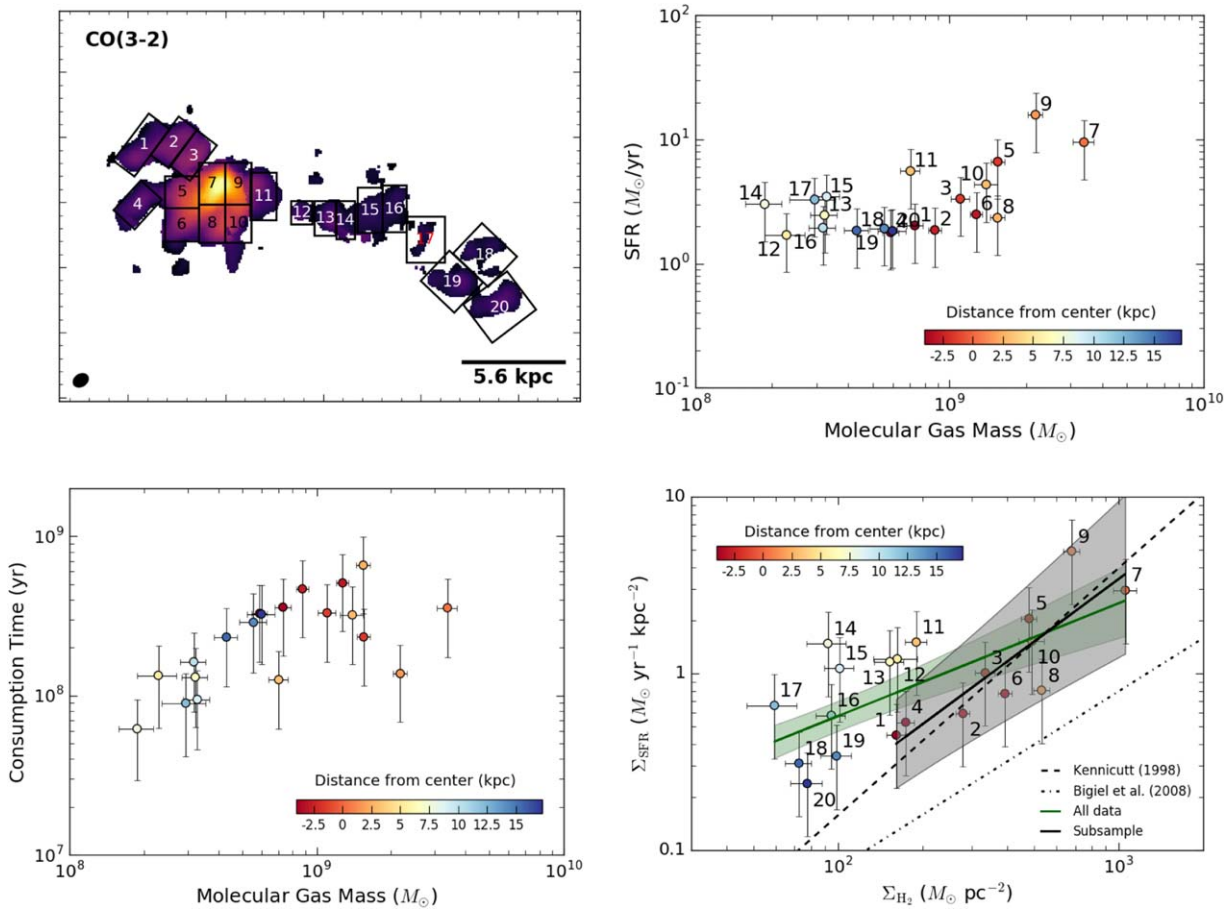

Figure 9. Relationship between molecular gas mass and SFR throughout the entire gas distribution. The top left panel shows the regions used to measure the molecular gas masses and SFRs, overlaid on the integrated CO (3–2) map. The top right panel shows the M_{mol}–SFR relation. The bottom left panel shows the local consumption timescale (M_{mol}/SFR) as a function of molecular gas mass. The bottom right panel expresses the SFR–M_{mol} relation in terms of surface densities. Each point is labeled with its identifier from the top left panel and is also colored by its distance from the BCG nucleus. Negative distances correspond to points east of the nucleus. The bottom panel shows two fits to the Σ_{SFR}–Σ_{H_2} relation. The first (green) includes all of the data. The second (gray) excludes regions 11–17, which correspond to the inner and middle portions of the filament. The shaded regions correspond to the 1σ error bounds for the best fits. The relations from Kennicutt (1998) and Bigiel et al. (2008) are also plotted.

(e.g., Donahue et al. 2015; Fogarty et al. 2015) had a negligible effect on this SFR. Assuming that the current SFR persists, the $1.9 \times 10^{10}\,M_\odot$ of cold gas in the BCG will be consumed in 1.4×10^{8} yr. This consumption time (M_{mol}/SFR) is comparable to those of starbursts and other BCGs (e.g., Donahue et al. 2015).

We used this global SFR to calibrate local measurements along the filament. The FUV count rates in the *HST* F165LP image were extracted from the regions shown in Figure 9 (top left), which were background-subtracted using a large, source-free region within the field of view. The FUV count rate was also extracted from a large box containing all of the observed emission. Local SFRs were then computed by assuming that the UV count rates translate linearly to SFR (e.g., Kennicutt 1998; Salim et al. 2007), with the total UV count rate fixed to the global SFR. Thus, the SFR within each region is the ratio of its UV count rate to the total UV count rate multiplied by the global SFR. Note that the total UV luminosity was converted to a global SFR using the Salim et al. (2007) relation, which assumes a Chabrier initial mass function and is 30% lower than the Kennicutt (1998) conversion.

The quoted SFR has been corrected for both Galactic extinction and dust extinction intrinsic to the BCG. No attempt has been made to correct for local variations in dust extinction. Based on the maps presented in Ogrean et al. (2010), the SFR in the nucleus may be underestimated by ∼40%, while the SFR at large radii may be overestimated by ∼20%. Throughout this work we take the SFR uncertainty to be a factor of two, which is the approximate accuracy of the SFR calibration. The statistical uncertainties in the local SFRs are small compared to the systematic uncertainty in the global SFR calibration. Spatial variations in dust extinction therefore shift the data points by less than their uncertainty.

Figure 9 also presents the SFR and consumption timescale as a function of molecular gas mass, as well as the relation between star formation and molecular gas surface densities. Surface densities were determined by dividing the appropriate quantity by the area of the extraction region. Each point has been labeled according to the numbers shown in the top left panel of Figure 9 and color-coded by its distance from the BCG nucleus, with negative distances corresponding to eastward points.

The relationship between SFR and molecular gas mass is flat for $M_{mol} < 10^9\,M_\odot$ and increases approximately linearly for higher masses. These two regimes are well separated by their location within the cluster. Regions with high M_{mol} are located at the center of the BCG, while the lower-mass regions are

situated along the filament. In the outer filament, which joins the flat and approximately linear regimes in the $M_{\rm mol}$–SFR relation, the molecular gas and UV emission are slightly offset (see Figure 5). We have used regions large enough to include both the molecular gas and UV emission. Choosing instead regions that are confined to the molecular gas reduces the SFR so that it is consistent with the linear relation present at higher masses. The consumption timescale (middle panel) for the central gas is roughly constant, with a mean of $3.7 \pm 1.4 \times 10^8$ yr. Since the filamentary gas has a constant SFR, its consumption time increases with $M_{\rm mol}$, with a mean of $1.6 \pm 0.8 \times 10^8$ yr.

The star formation law in spiral and starburst galaxies is well characterized by the Kennicutt–Schmidt (KS) relation (Kennicutt 1998; Kennicutt & Evans 2012), which takes the form

$$\left(\frac{\Sigma_{\rm SFR}}{M_\odot\ {\rm yr}^{-1}\,{\rm kpc}^{-2}}\right) = 2.5 \times 10^{-4}\left(\frac{\Sigma_{\rm gas}}{M_\odot\ {\rm pc}^{-2}}\right)^{1.4}. \quad (10)$$

This expression relates the gas (H I+H_2) surface density, $\Sigma_{\rm gas}$, to the SF surface density, $\Sigma_{\rm SFR}$, over 5 and 7 decades, respectively. When a dense gas tracer is used in lieu of the total gas surface density, the SF law scales linearly (Wu et al. 2005). This is because dense gas tracers probe the gas directly involved in star formation. Spatially resolved observations of spiral galaxies that use $\Sigma_{\rm H_2}$ alone have also recovered a linear scaling (Bigiel et al. 2008).

We have modeled the spatially resolved SF law in RXC J1504 using the functional form

$$\left(\frac{\Sigma_{\rm SFR}}{M_\odot\ {\rm yr}^{-1}\,{\rm kpc}^{-2}}\right) = A\left(\frac{\Sigma_{\rm H_2}}{100\ M_\odot\ {\rm pc}^{-2}}\right)^{N}, \quad (11)$$

which uses the molecular gas surface density, $\Sigma_{\rm H_2}$, instead of the total gas surface density. At the centers of clusters the confining pressure is high enough to convert $\gtrsim$95% of the gas into molecular form (Blitz & Rosolowsky 2006). The fits were conducted in log space using the LINMIX package in Python, which employs the Bayesian approach to linear regression described in Kelly (2007). By centering $\Sigma_{\rm H_2}$ at 100 $M_\odot$ pc^{-2}, we obtain more appropriate uncertainties.

Fitting this star formation law to the entire gas distribution yields $A = 0.58 \pm 0.11$ and $N = 0.64 \pm 0.18$. The best fit and its 1σ error bounds are shown in green in Figure 9. This scaling is significantly flatter than the nominal $N = 1.4 \pm 0.2$ measured in spirals and starbursts. Restricting the fits to the central gas (regions 1–10) gives $A = 0.23 \pm 0.13$ and $N = 1.18 \pm 0.37$, shown as a black line with gray shaded area in Figure 9. The large uncertainties result from the small dynamic range in $\Sigma_{\rm H_2}$. This is consistent with both a KS and linear scaling. Overplotting the KS relation on Figure 9 (dashed black line) passes directly through this subset of the data. Along the filament $\Sigma_{\rm SFR}$ is systematically higher. The clumps in the outer filament are marginally consistent with lying on the KS relation. Incorporating these regions (18–20) into the fit to the star formation law yields $N = 0.98 \pm 0.18$. $\Sigma_{\rm SFR}$ along the middle filament is even higher, lying well above the mean KS relation with significant scatter.

The linear scaling measured between $\Sigma_{\rm SFR}$ and $\Sigma_{\rm H_2}$ in spiral galaxies (Bigiel et al. 2008) has also been plotted in Figure 9. Although the scaling is consistent with that of the central gas, and is even better matched to the data when the outer filament is included in the fit, the normalization lies below that in RXC J1504. Assuming that these systems share the same intrinsic SF law when expressed in terms of dense gas mass (i.e., $\Sigma_{\rm SFR} \propto \Sigma_{\rm dense}$), the difference between them can be attributed to the fraction of molecular gas concentrated within the dense cores. Reconciling the two normalizations requires that the fraction of gas in the dense cores is 3–4 times higher in RXC J1504 than in spirals. The additional confining pressure of the hot atmosphere could be responsible for compressing the molecular clouds. Indeed, the confining pressure dictates the conversion between atomic and molecular gas (e.g., Blitz & Rosolowsky 2006) and should also influence the prevalence of dense clumps.

The enhanced SFR throughout the majority of the filament indicates that either it is not located on the KS relation or it is affected by systematic uncertainties. We cannot rule out either possibility with the existing data. In Section 3.5 we noted that the star formation and molecular gas do not coincide well in the middle and outer portions of the filament. Ongoing star formation could have consumed a portion of the local supply of molecular gas, leading to decreased molecular gas surface densities for the observed SFR. The primary systematic uncertainty is in the calibration of the molecular gas mass using the CO-to-H_2 conversion factor. Reconciling this population with the KS relation requires a fourfold increase in $M_{\rm mol}$. Elevated values of $X_{\rm CO}$ are often found in metal-poor molecular clouds. However, the middle and outer filaments should have similar metallicities, as they presumably both formed from the hot atmosphere, but their star formation efficiencies differ.

In Figure 10 we plot the ratio of consumption time to freefall time for each of the regions shown in Figure 9. The freefall time was computed from the mass profile presented in Section 4.2. This neglects the contribution from the cluster halo but is accurate within the central $\sim$20 kpc, where the molecular gas is located. In all regions the consumption time is longer than the freefall time. The ratio ranges from a factor of about 3 in the middle filament to $\sim$40 within the core. This indicates that the molecular gas should be relatively long-lived. Star formation will not churn through the molecular gas before it falls back onto the BCG.

Other mechanisms, such as photodissociation or evaporation by collisions with hot electrons, could still deplete the molecular gas. Similarly, reduced infall velocities resulting from ram pressure drag, as discussed in Section 4.2, will lengthen the time taken for a molecular cloud to fall onto the BCG. In the middle filament, where the consumption time is shortest, this can result in an infall time longer than the consumption time, so that the gas is consumed before it reaches the galactic center.

If the molecular gas survives long enough to return to the galactic center, then it should settle into a rotationally supported structure, such as a ring or disk, in a few dynamical times. The lack of such a structure suggests that the molecular gas either is dynamically young, having not yet had time to form a disk, or is continually destroyed and reformed within the central galaxy, with the warmer phase experiencing enough nongravitational motion to prevent it from forming a disk.

5. Conclusions

In this work, we have presented ALMA observations of the CO (1–0) and CO (3–2) emission lines in the BCG of the RXC J1504–0248 galaxy cluster. This is one of the most

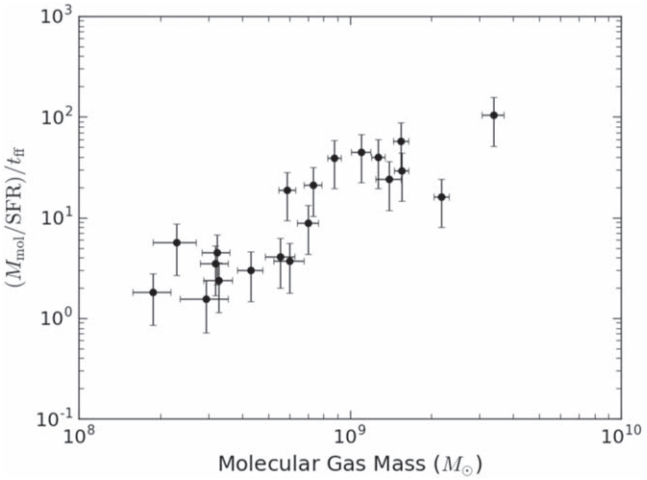

Figure 10. Ratio of the consumption timescale ($M_{\rm mol}$/SFR) to the freefall time for each of the regions shown in Figure 9.

extreme cool core clusters known. The BCG contains $1.9 \pm 0.1 \times 10^{10}\,M_\odot$ of molecular gas that has a complex and disturbed morphology. It is distributed between three distinct structures. The first is a pair of redshifted clumps located within the central 5 kpc of the radio source at the galactic nucleus. Next, a 20 kpc long filament, containing $4.8 \times 10^9\,M_\odot$ of cold gas, extends radially to the southwest of the nucleus. Finally, coincident with the AGN is an unresolved structure that is both broader (400 km s^{-1} FWHM) and more blueshifted ($v \approx -250$ km s^{-1}) than the rest of the gas in the BCG. We find no evidence of a long-lived, rotationally supported structure. Instead, the gas is apparently dynamically young.

The molecular gas has almost certainly formed from the condensation of the ICM. Alternative mechanisms, such as repeated minor mergers or tidal stripping, are implausible. Moreover, the presence of molecular gas and star formation in BCGs is linked to short central cooling times in their hot atmospheres. The molecular filament in RXC J1504 is oriented along the edge of both a ridge of bright X-ray emission and a putative X-ray cavity. The cavity is energetic enough to stimulate the production of molecular gas by lifting low-entropy gas from the cluster center to a radius where it becomes thermally unstable. As the filament does not trail directly behind the cavity, this interpretation is not as clear-cut as in other BCGs with molecular filaments.

The velocity gradient along the filament is smooth and shallow. The velocity shear implies a flow rate of 75 $M_\odot$ yr^{-1}. Models of gravitational freefall can reproduce the velocity gradient as long as the filament lies within 20° of the plane of the sky. Assuming that the molecular gas in the outermost clumps fills their volume, then their mean densities are too high to be slowed by ram pressure. However, low velocities and comparably shallow velocity gradients are common in BCGs. This suggests that molecular clouds are likely moving at sub-freefall velocities, instead of the filaments in many systems lying close to the plane of the sky. Lower terminal velocities can be attained if the mean density of the molecular clouds is reduced. This would be the case if the molecular clouds are tied to a warm, diffuse, volume-filling phase that is susceptible to ram pressure drag.

Filamentary blue and ultraviolet emission in the BCG traces a young stellar population formed at a rate of 136 $M_\odot$ yr^{-1}. This emission is coincident with both the nuclear gas and the molecular filament. Persisting at its current rate, star formation will consume the molecular gas in 1.4×10^8 yr. This timescale is comparable to both the central cooling time (2.3×10^8 yr) and the time required for mass deposition from the ICM to build up the observed reservoir of cold gas (2.4×10^8 yr). Star formation near the cluster core is consistent with the KS law. The filament exhibits increased star formation surface densities, possibly resulting from the consumption of a finite molecular gas supply. Alternatively, spatial variations in the CO-to-H_2 conversion factor could introduce systematic variations in the molecular gas surface density.

We thank the anonymous referee for helpful comments that improved the paper. Support for this work was provided in part by the National Aeronautics and Space Administration through *Chandra* award no. G08-19109A issued by the Chandra X-ray Center, which is operated by the Smithsonian Astrophysical Observatory for and on behalf of the National Aeronautics Space Administration under contract NAS8-03060. A.N.V. and B.R.M. acknowledge support from the Natural Sciences and Engineering Research Council of Canada. B.R.M. further acknowledges support from the Canadian Space Agency Space Science Enhancement Program. This paper makes use of the ALMA data ADS/JAO.ALMA 2016.1.01269.S. ALMA is a partnership of the ESO (representing its member states), NSF (USA), and NINS (Japan), together with NRC (Canada), NSC and ASIAA (Taiwan), and KASI (Republic of Korea), in cooperation with the Republic of Chile. The Joint ALMA Observatory is operated by ESO, AUI/NRAO, and NAOJ. This research made use of Astropy, a community-developed core Python package for Astronomy. This research made use of APLpy, an open-source plotting package for Python hosted at http://aplpy.github.com.

Software: Astropy, Matplotlib, Aplpy, lmfit.

ORCID iDs

A. N. Vantyghem https://orcid.org/0000-0003-4227-4838
B. R. McNamara https://orcid.org/0000-0002-2622-2627
A. C. Edge https://orcid.org/0000-0002-3398-6916
P. E. J. Nulsen https://orcid.org/0000-0003-0297-4493
F. Combes https://orcid.org/0000-0003-2658-7893
A. C. Fabian https://orcid.org/0000-0002-9378-4072
M. McDonald https://orcid.org/0000-0001-5226-8349

References

Abazajian, K., Adelman-McCarthy, J. K., Agüeros, M. A., et al. 2004, AJ, 128, 502
Bauer, F. E., Condon, J. J., Thuan, T. X., & Broderick, J. J. 2000, ApJS, 129, 547
Bell, E. F., McIntosh, D. H., Katz, N., & Weinberg, M. D. 2003, ApJS, 149, 289
Bigiel, F., Leroy, A., Walter, F., et al. 2008, AJ, 136, 2846
Bîrzan, L., Rafferty, D. A., McNamara, B. R., Wise, M. W., & Nulsen, P. E. J. 2004, ApJ, 607, 800
Bîrzan, L., Rafferty, D. A., Nulsen, P. E. J., et al. 2012, MNRAS, 427, 3468
Blitz, L., & Rosolowsky, E. 2006, ApJ, 650, 933
Böhringer, H., Burwitz, V., Zhang, Y.-Y., Schuecker, P., & Nowak, N. 2005, ApJ, 633, 148
Bolatto, A. D., Wolfire, M., & Leroy, A. K. 2013, ARA&A, 51, 207
Bourda, G., Charlot, P., Porcas, R. W., & Garrington, S. T. 2010, A&A, 520, A113
Canning, R. E. A., Sun, M., Sanders, J. S., et al. 2013, MNRAS, 435, 1108
Cavagnolo, K. W., Donahue, M., Voit, G. M., & Sun, M. 2008, ApJL, 683, L107

Cavagnolo, K. W., McNamara, B. R., Nulsen, P. E. J., et al. 2010, ApJ, 720, 1066
Cavaliere, A., & Fusco-Femiano, R. 1976, A&A, 49, 137
Conselice, C. J., Gallagher, J. S., III, & Wyse, R. F. G. 2001, AJ, 122, 2281
Cowie, L. L., Hu, E. M., Jenkins, E. B., & York, D. G. 1983, ApJ, 272, 29
Crawford, C. S., Allen, S. W., Ebeling, H., Edge, A. C., & Fabian, A. C. 1999, MNRAS, 306, 857
David, L. P., Lim, J., Forman, W., et al. 2014, ApJ, 792, 94
Donahue, M., Connor, T., Fogarty, K., et al. 2015, ApJ, 805, 177
Dunn, R. J. H., & Fabian, A. C. 2006, MNRAS, 373, 959
Dunn, R. J. H., Fabian, A. C., & Taylor, G. B. 2005, MNRAS, 364, 1343
Edge, A. C. 2001, MNRAS, 328, 762
Edge, A. C., & Frayer, D. T. 2003, ApJL, 594, L13
Edge, A. C., Wilman, R. J., Johnstone, R. M., et al. 2002, MNRAS, 337, 49
Fabian, A. C., Johnstone, R. M., Sanders, J. S., et al. 2008, Natur, 454, 968
Fabian, A. C., Sanders, J. S., Crawford, C. S., et al. 2003, MNRAS, 344, L48
Fabian, A. C., Sanders, J. S., Ettori, S., et al. 2001, MNRAS, 321, L33
Fabian, A. C., Sanders, J. S., Taylor, G. B., et al. 2006, MNRAS, 366, 417
Fabian, A. C., Sanders, J. S., Williams, R. J. R., et al. 2011, MNRAS, 417, 172
Ferland, G. J., Fabian, A. C., Hatch, N. A., et al. 2009, MNRAS, 392, 1475
Fogarty, K., Postman, M., Connor, T., Donahue, M., & Moustakas, J. 2015, ApJ, 813, 117
Gaspari, M., McDonald, M., Hamer, S. L., et al. 2018, ApJ, 854, 167
Gaspari, M., Ruszkowski, M., & Oh, S. P. 2013, MNRAS, 432, 3401
Gaspari, M., Ruszkowski, M., & Sharma, P. 2012, ApJ, 746, 94
Gendron-Marsolais, M., Hlavacek-Larrondo, J., Martin, T. B., et al. 2018, MNRAS, 479, L28
Giacintucci, S., Markevitch, M., Brunetti, G., Cassano, R., & Venturi, T. 2011, A&A, 525, L10
Hamer, S. L., Edge, A. C., Swinbank, A. M., et al. 2014, MNRAS, 437, 862
Hatch, N. A., Crawford, C. S., Fabian, A. C., & Johnstone, R. M. 2005, MNRAS, 358, 765
Hatch, N. A., Crawford, C. S., Johnstone, R. M., & Fabian, A. C. 2006, MNRAS, 367, 433
Heckman, T. M. 1981, ApJL, 250, L59
Hernquist, L. 1990, ApJ, 356, 359
Hitomi Collaboration, Aharonian, F., Akamatsu, H., et al. 2016, Natur, 535, 117
Hogan, M. T., McNamara, B. R., Pulido, F., et al. 2017, ApJ, 837, 51
Hu, E. M., Cowie, L. L., & Wang, Z. 1985, ApJS, 59, 447
Kelly, B. C. 2007, ApJ, 665, 1489
Kennicutt, R. C., Jr. 1998, ARA&A, 36, 189
Kennicutt, R. C., & Evans, N. J. 2012, ARA&A, 50, 531
Kirkpatrick, C. C., McNamara, B. R., Rafferty, D. A., et al. 2009, ApJ, 697, 867
Li, Y., & Bryan, G. L. 2014, ApJ, 789, 153
Li, Y., Ruszkowski, M., & Bryan, G. L. 2017, ApJ, 847, 106
Li, Y., Ruszkowski, M., & Tremblay, G. 2018, ApJ, 854, 91
Lim, J., Ao, Y., & Dinh-V-Trung 2008, ApJ, 672, 252
Lim, J., Ohyama, Y., Chi-Hung, Y., Dinh-V-Trung, & Shiang-Yu, W. 2012, ApJ, 744, 112
Lynds, R. 1970, ApJL, 159, 151L
McCourt, M., Sharma, P., Quataert, E., & Parrish, I. J. 2012, MNRAS, 419, 3319
McDonald, M., Veilleux, S., & Rupke, D. S. N. 2012, ApJ, 746, 153
McDonald, M., Veilleux, S., Rupke, D. S. N., Mushotzky, R., & Reynolds, C. 2011, ApJ, 734, 95
McMullin, J. P., Waters, B., Schiebel, D., Young, W., & Golap, K. 2007, in ASP Conf. Ser. 376, Astronomical Data Analysis Software and Systems XVI, ed. R. A. Shaw, F. Hill, & D. J. Bell (San Francisco, CA: ASP), 127
McNamara, B. R. 2004, in The Riddle of Cooling Flows in Galaxies and Clusters of Galaxies, ed. T. Reiprich, J. Kempner, & N. Soker (Charlottesville, VA: Univ. Virginia), 177
McNamara, B. R., & Nulsen, P. E. J. 2007, ARA&A, 45, 117
McNamara, B. R., & Nulsen, P. E. J. 2012, NJPh, 14, 055023
McNamara, B. R., Russell, H. R., Nulsen, P. E. J., et al. 2014, ApJ, 785, 44
McNamara, B. R., Russell, H. R., Nulsen, P. E. J., et al. 2016, ApJ, 830, 79
O'Dea, C. P., Baum, S. A., Privon, G., et al. 2008, ApJ, 681, 1035
Ogrean, G. A., Hatch, N. A., Simionescu, A., et al. 2010, MNRAS, 406, 354
Panagoulia, E. K., Fabian, A. C., Sanders, J. S., & Hlavacek-Larrondo, J. 2014, MNRAS, 444, 1236
Petrov, L. 2013, AJ, 146, 5
Pizzolato, F., & Soker, N. 2005, ApJ, 632, 821
Pizzolato, F., & Soker, N. 2010, MNRAS, 408, 961
Poggianti, B. M. 1997, A&AS, 122, arXiv:astro-ph/9608029
Prasad, D., Sharma, P., & Babul, A. 2015, ApJ, 811, 108
Protassov, R., van Dyk, D. A., Connors, A., Kashyap, V. L., & Siemiginowska, A. 2002, ApJ, 571, 545
Pulido, F. A., McNamara, B. R., Edge, A. C., et al. 2017, ApJ, 853, 177
Rafferty, D. A., McNamara, B. R., & Nulsen, P. E. J. 2008, ApJ, 687, 899
Rafferty, D. A., McNamara, B. R., Nulsen, P. E. J., & Wise, M. W. 2006, ApJ, 652, 216
Revaz, Y., Combes, F., & Salomé, P. 2008, A&A, 477, L33
Russell, H. R., McDonald, M., McNamara, B. R., et al. 2017, ApJ, 836, 130
Russell, H. R., McNamara, B. R., Edge, A. C., et al. 2014, ApJ, 784, 78
Russell, H. R., McNamara, B. R., Fabian, A. C., et al. 2016, MNRAS, 458, 3134
Salim, S., Rich, R. M., Charlot, S., et al. 2007, ApJS, 173, 267
Salomé, P., & Combes, F. 2003, A&A, 412, 657
Salomé, P., Combes, F., Edge, A. C., et al. 2006, A&A, 454, 437
Salomé, P., Combes, F., Revaz, Y., et al. 2011, A&A, 531, A85
Schlafly, E. F., & Finkbeiner, D. P. 2011, ApJ, 737, 103
SDSS Collaboration, Albareti, F. D., Allende Prieto, C., et al. 2017, ApJS, 233, 25
Sharma, P., McCourt, M., Quataert, E., & Parrish, I. J. 2012, MNRAS, 420, 3174
Solomon, P. M., Rivolo, A. R., Barrett, J., & Yahil, A. 1987, ApJ, 319, 730
Solomon, P. M., & Vanden Bout, P. A. 2005, ARA&A, 43, 677
Tremblay, G. R., O'Dea, C. P., Baum, S. A., et al. 2015, MNRAS, 451, 3768
Vantyghem, A. N., McNamara, B. R., Edge, A. C., et al. 2017, ApJ, 848, 101
Vantyghem, A. N., McNamara, B. R., Russell, H. R., et al. 2014, MNRAS, 442, 3192
Vantyghem, A. N., McNamara, B. R., Russell, H. R., et al. 2016, ApJ, 832, 148
Véron-Cetty, M.-P., & Véron, P. 2010, A&A, 518, A10
Walker, S. A., Kosec, P., Fabian, A. C., & Sanders, J. S. 2015, MNRAS, 453, 2480
Werner, N., Oonk, J. B. R., Canning, R. E. A., et al. 2013, ApJ, 767, 153
Werner, N., Oonk, J. B. R., Sun, M., et al. 2014, MNRAS, 439, 2291
Werner, N., Sun, M., Bagchi, J., et al. 2011, MNRAS, 415, 3369
Wu, J., Evans, N. J., II, Gao, Y., et al. 2005, ApJL, 635, L173
Young, L. M., Bureau, M., Davis, T. A., et al. 2011, MNRAS, 414, 940